Tuning magnetism and band topology through antisite defects in Sb-doped MnBi4Te7

Chaowei Hu,[1,*] Shang-Wei Lien,[2,*] Erxi Feng,[3] Scott Mackey [1] Hung-Ju Tien,[2] Igor I. Mazin,[4] Huibo Cao,[3]
Tay-Rong Chang,[2,5,6,†] and Ni Ni [1,‡]

[1]*Department of Physics and Astronomy and California NanoSystems Institute, University of California, Los Angeles, California 90095, USA*
[2]*Department of Physics, National Cheng Kung University, Tainan 701, Taiwan*
[3]*Neutron Scattering Division, Oak Ridge National Laboratory, Oak Ridge, Tennessee 37831, USA*
[4]*Department of Physics and Astronomy, and Center of Quantum Science and Engineering, George Mason University,
Fairfax, Virginia 22030, USA*
[5]*Center for Quantum Frontiers of Research and Technology (QFort), Tainan 701, Taiwan*
[6]*Physics Division, National Center for Theoretical Sciences, Taipei 10617, Taiwan*

The fine control of magnetism and electronic structure in a magnetic topological insulator is crucial in order to realize various novel magnetic topological states including axion insulators, magnetic Weyl semimetals, Chern insulators, etc. Through crystal growth, transport, thermodynamic, neutron diffraction measurements, we show that under Sb doping the newly discovered intrinsic antiferromagnetic (AFM) topological insulator MnBi4Te7 evolves from AFM to ferromagnetic (FM) and then ferrimagnetic. We attribute this to the formation of $Mn_{(Bi,Sb)}$ antisites upon doping, which results in additional Mn sublattices that modify the delicate interlayer magnetic interactions and cause the dominant Mn sublattice to go from AFM to FM. We further investigate the effect of antisites on the band topology using the first-principles calculations. Without considering antisites, the series evolves from AFM topological insulator ($x = 0$) to FM axion insulators. In the exaggerated case of 16.7% of periodic antisites, the band topology is modified and a type-I magnetic Weyl semimetal phase can be realized at intermediate dopings. Therefore, this doping series provides a fruitful platform with continuously tunable magnetism and topology for investigating emergent phenomena, including quantum anomalous Hall effect, Fermi arc states, etc.

I. INTRODUCTION

Magnetic topological material provides a great platform in discovering new topological states, such as axion insulators, magnetic Weyl semimetals, and Chern insulators [1]. Emergent phenomena including quantum anomalous Hall (QAH) effect and quantized magnetoelectric effect have been proposed or observed in these phases, offering unprecedented technological opportunities to low-energy-consumption devices, quantum metrology, and quantum computing [2–4]. Recently, MnBi$_{2n}$Te$_{3n+1}$ (MBT) series are shown to be intrinsic magnetic topological insulators (MTIs), where the QAH effect was observed [5–35]. They are made of alternating $n - 1$ quintuple-layered (QL) blocks of [Bi2Te3] and one septuple layer (SL) of [MnBi2Te4]. The great structural tunability and natural heterostructural nature of MBT have made it a rare and unique platform to study the interplay among magnetism, band topology, electron correlations, and crystal structure. By reducing the interlayer coupling with increasing n and thus the interlayer Mn-Mn distance, MBT evolves from a Z_2 A-type AFM TI with saturation fields of

8 T in MnBi2Te4 ($n = 1$) [9,15,16], 0.22 T in MnBi4Te7 ($n = 2$) [11,20], and 0.18 T in MnBi6Te10 ($n = 3$) [28–31] to a ferromagnetic (FM) axion insulator in MnBi8Te13 ($n = 4$) [12]. Continuous tuning of magnetism and band topology was achieved in Sb-doped MnBi2Te4 [19,36,37]. This series goes from the AFM TI state in MnBi2Te4 to a likely trivial ferrimagnetic state in MnSb2Te4 where an additional Mn sublattice arises from the $Mn_{(Bi,Sb)}$ antisite defects [36,38–40]. Moreover, angle-resolved photoemission spectroscopy (ARPES) measurements reveal that even 7.5% of Sb doping induces a sizable surface gap opening in MnBi2Te4 [37]. The delicate energy-scale competition was further demonstrated in MnSb2Te4 [39]. While both Mn sublattices always couple antiferromagnetically, in samples with slightly lower (higher) Mn_{Sb} antisite defects, each Mn sublattice orders antiferromagnetically (ferromagnetically) [39].

Compared to MnBi2Te4, the AFM and FM ground states can be closer in energy in high n MBT members due to the larger Mn-Mn interlayer distance. Moreover, additional Mn sublattices will arise from the antisites in QLs upon doping [40]. Therefore, the high n MBT members will be more sensitive to perturbations. Indeed, 30% of Sb doping makes MnBi6Te10 FM [41]. However, due to the lack of intermediate doping levels, it is unclear how the magnetism and band topology develop in the high n members. Here we report the study of the effect of Sb doping on MnBi4Te7 and reveal the

*These authors contributed equally to this work.
†Corresponding author: u32trc00@phys.ncku.edu.tw
‡Corresponding author: nini@physics.ucla.edu

important role of the $Mn_{(Bi,Sb)}$ antisites upon Sb doping in governing the magnetism and band topology.

II. METHODS

Single crystals were grown using the flux method [11,16]. Elemental forms of Mn, Bi, Sb, and Te are mixed at the ratio of $MnTe : (Bi_{1-x}Sb_x)_2Te_3 = 15 : 85$ in an alumina crucible sealed in a quartz ampule under $1/3$ atm of argon. The quartz ampule is quickly heated to $900\,°C$ and stays for 5 h, followed by a quick cooling to $10°$ above the targeted spin-out temperature. Then it is slowly cooled to the spin-out temperature over three days and stays for another three days before the spin out. Since each of the doped samples has a very narrow but different growth temperature window, similar trial-and-error growth strategy to the one for $MnBi_8Te_{13}$ was used to determine the spin-out temperature here [12]. Mn-doped Bi_2Te_3 (023 phase) can intergrow with the targeted phase and may contaminate the intrinsic properties. Therefore, extra care was paid to select the best pieces for the study. First, x-ray diffraction at low angles for both the top and bottom (00l) surfaces were measured to select the ones without the 023 phase on the surface. Then, a part of the selected piece was ground for the powder x-ray diffraction (PXRD) to further screen the samples without the 023 impurities. Finally, all measurements were performed on the same piece. We found no significant piece-to-piece variation in magnetic properties within each batch.

Chemical analysis was obtained by the wavelength-dispersive spectroscopy (WDS) measurements performed on a JEOL JXA-8200 Superprobe. Thermodynamic measurement was performed using the QD Magnetic Properties Measurement System (QD MPMS3). Electric transport measurement was performed using the standard six-probe configuration using the Quantum Design Dynacool Physical Properties Measurement System (QD Dynacool PPMS). To eliminate unwanted contributions from mixed transport channels of the magnetotransport data, data were collected while sweeping the magnetic field from -9 T to 9 T. The data were then symmetrized to obtain $\rho_{xx}(B)$ using $\rho_{xx}(B) = \frac{\rho_{xx}(B) + \rho_{xx}(-B)}{2}$ and antisymmetrized to get $\rho_{xy}(B)$ using $\rho_{xy}(B) = \frac{\rho_{xy}(B) - \rho_{xy}(-B)}{2}$. The sign of ρ_{xy} is chosen so that hole carriers lead to positive ρ_{xy}.

Single-crystal neutron diffraction was performed for the $x = 0.76$ sample at 5 K and 50 K at 0 T on the HB-3A DE-MAND single-crystal neutron diffractometer located at Oak Ridge National Laboratory [42]. Neutron wavelength of 1.551 Å was selected by a bent perfect Si-220 monochromator. The nuclear and magnetic structures were subsequently refined with the FULLPROF SUITE software [43].

We computed the electronic structures using the projector augmented wave method [44,45] as implemented in the VASP package [46] within the generalized gradient approximation schemes (GGA) [47] and GGA plus Hubbard U (GGA + U) [48] scheme. On-site $U = 5.0$ eV was used for Mn d orbitals. An $11 \times 11 \times 5$ MonkhorstPack k-point mesh was used in the computations. The spin-orbit coupling effects were included in calculations. The experimental lattice parameters were used. The atomic positions were relaxed until the residual forces were less than 0.01 eV/Å. We used Mn d orbitals, Bi p
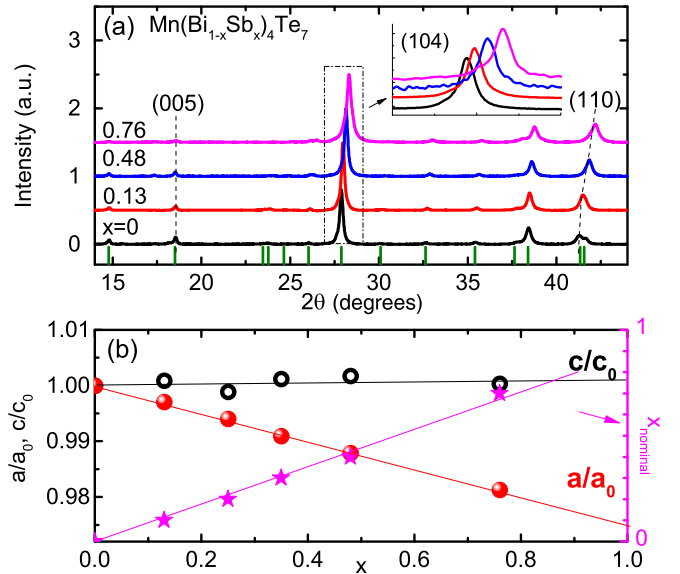

FIG. 1. (a) PXRD of $Mn(Bi_{1-x}Sb_x)_4Te_7$ for the pieces for which the data in the paper were collected. The peak positions of the 147 phase are marked. Inset: the zoom-in plot of the (104) PXRD peaks. (b) The doping-dependent relative lattice parameters a/a_0, c/c_0 and nominal concentration $x_{nominal}$ used in the growth. a_0 and c_0 are the lattice parameters for $MnBi_4Te_7$.

orbitals, Sb p orbitals, and Te p orbitals to construct Wannier functions, without performing the procedure for maximizing localization [49].

III. RESULTS

Both the PXRD and chemical analysis via WDS indicate that Sb was successfully doped into $MnBi_4Te_7$ and the results are summarized in Fig. 1 and Table I. Figure 1(a) shows the PXRD patterns for various doping levels. All peaks can be indexed by the 147 phase. If there is 023 phase impurity, a clear hump will appear at the left shoulder of the (104) peak. As shown in the inset of Fig. 1(a), the 023 phase is indiscernible or less than 5% if there is. With Sb doping, the (005) peak roughly stays at the same angle, while the (104) peak shifts moderately and the (110) peak shifts much to higher angles, indicating distinct in-plane and out-of-plane lattice response to the Sb doping. Figure 1(b) shows the doping-dependent lattice evolution. The lattice parameter a decreases linearly by 2% up to our highest doping level $x = 0.76$, while the lattice parameter c remains almost the same. This lattice evolution is similar to that in $Mn(Bi_{1-x}Sb_x)_2Te_4$ [36].

WDS reveals the real doping level of Sb as well as a universal deficiency of Mn in all compounds as seen in Table I. The total Mn concentration is near 0.8 for all but slowly increases with x. This is because, when Sb substitutes Bi, it also introduces the preferable Mn_{Sb} antisites [36,38–40] (high-spin Mn^{2+} ionic radius, 99 pm, is closer to that of Sb^{3+}, 90 pm, than to Bi^{3+}, 117 pm [50]). Therefore, upon Sb doping, more and more Mn can enter into the Bi/Sb sites. In contrast to the $Mn(Bi_{1-x}Sb_x)_2Te_4$ series where two Mn sublattices exist due to the $Mn_{(Bi,Sb)}$ antisite formation, Sb doping in $MnBi_4Te_7$ gives rise to a more complex antisite chemistry, where three

TABLE I. Chemical composition of Sb-doped Mn-147, the estimation of defects concentration with m, n, and l representing the Mn occupancy on Mn2 sites, Mn occupancy on Mn3 sites, and Mn occupancy on Mn1 sites (see text). The uniaxial anisotropy parameter SD is estimated from Fig. 3(a)–3(d) (see text).

	$x_{nominal}$	Mn : Bi : Sb : Te	Sb/(Bi+Sb)	m	n	l	SD (meV)
WDS	0	0.78(3) : 4.27(7) : 0 : 7	0	0.015(5)	0.03(1)	0.73(3)	0.052
	0.1	0.79(2) : 3.70(3) : 0.57(1) : 7	0.13(1)	0.020(5)	0.04(1)	0.70(3)	0.053
	0.4	0.81(4) : 2.19(5) : 2.04(1) : 7	0.48(1)	0.025(5)	0.055(10)	0.65(3)	0.026
	0.7	0.82(1) : 1.00(3) : 3.08(2) : 7	0.76(1)	0.060(5)	0.07(1)	0.56(3)	0.015
Neutron	0.7	0.88(3): 1.15(6) : 2.96(6) : 7	0.72(2)	0.06(1)	0.07	0.62(1)	0.015

Mn sublattices appear. We denote the Mn atoms occupying the Mn site as Mn1 sublattice, the Mn atoms on the Bi site within SLs as Mn2 sublattice, and the Mn atoms on the Bi site in QLs as Mn3 sublattice; see Fig. 1 in [11]. As we will show later, while the Mn2 and Mn3 antisites are much less concentrated than Mn1, they do make a big impact on the overall magnetism and band topology.

A. Evolution of magnetism

Physical properties of the doping series are summarized in Figs. 2 and 3. The evolution of magnetic structure in the series can be well traced in the temperature-dependent susceptibility with $H \| c$ [$\chi^c(T)$] and the temperature-dependent resistivity with $I \| ab$ [$\rho_{xx}(T)$] and $I \| c$ [$\rho_{zz}(T)$], as well as the temperature-dependent specific heat [$C_p(T)$] data in Fig. 2. For $x = 0$, at $T_N = 12.7$ K, the sharp cusp in $\chi^c(T)$ and the kink in $C_p(T)$ signal the paramagnetic (PM) to AFM phase transition. Furthermore, below T_N, the sudden increase of $\rho_{zz}(T)$ and drop of $\rho_{xx}(T)$ are indicative of the gain (loss) of the spin-disorder scattering along the c axis (ab plane). This suggests spins parallel in the ab plane but antiparallel along the c axis, consistent with the A-type AFM structure revealed by neutron data [27,30].

For $x = 0.13$, in addition to a sharp cusp at $T_N = 12.8$ K in $\chi^c(T)$ suggesting AFM transition like the parent compound, a second transition occurs at $T_C = 6.0$ K marked by a sudden increase and a large bifurcation in the ZFC and FC data of $\chi^c(T)$. From T_N to T_C, $\rho_{zz}(T)$ increases sharply and $\rho_{xx}(T)$ drops, analogous to that of the $x = 0$ sample, while below T_C, $\rho_{zz}(T)$ decreases sharply due to the loss of spin scattering like that in the FM $MnBi_8Te_{13}$ [12]. Meanwhile, since Mn1 and Mn2 sublattices in the SL plane are strongly AFM coupled to each other through superexchange interaction [39], the Mn2 sublattice most likely orders simultaneously and antiferromagnetically with Mn1 at T_N. Therefore, we argue that, from
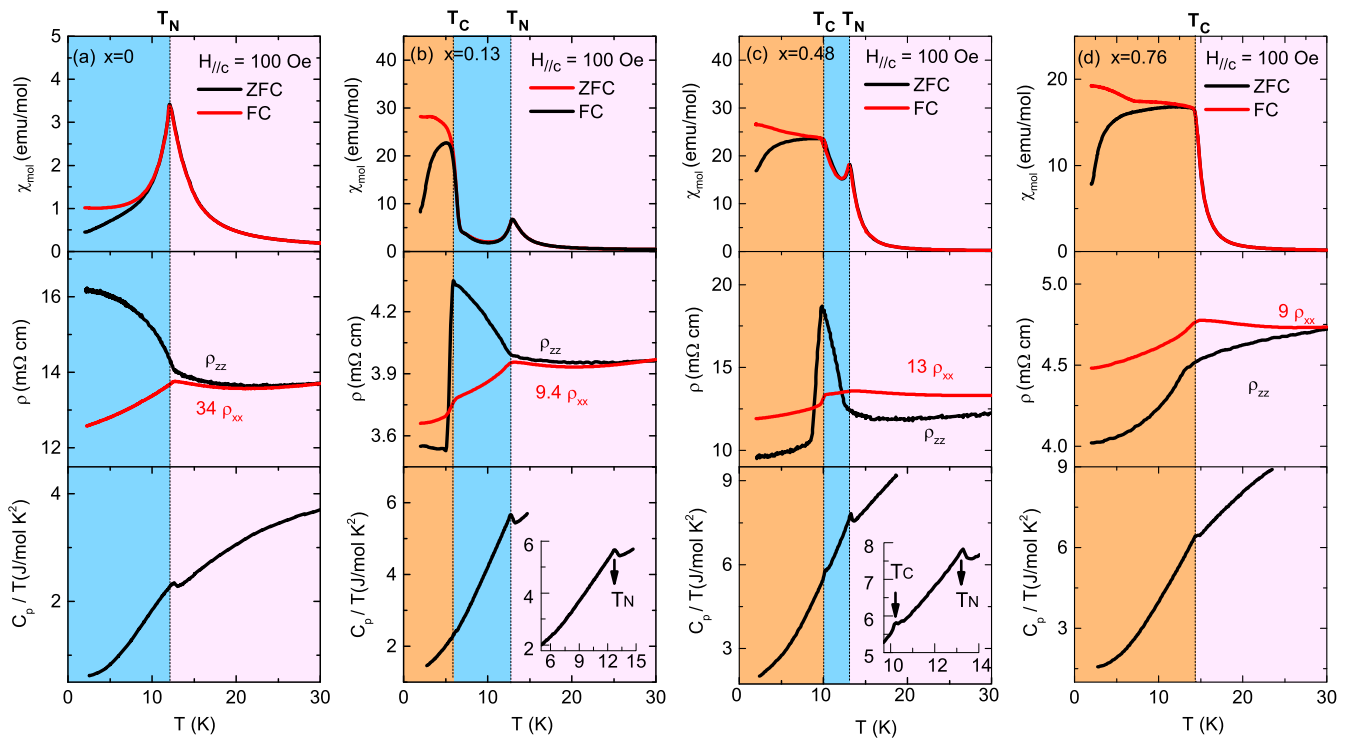

FIG. 2. Evolution of magnetism with temperature in $Mn(Bi_{1-x}Sb_x)_4Te_7$ from $x = 0$ to $x = 0.76$. (a)–(d) Top panel: $\chi^c(T)$, the temperature-dependent zero-field-cooled (ZFC) and field-cooled (FC) magnetic susceptibility under 0.01 T with $H \| c$. Middle panel: $\rho_{xx}(T)$ and $\rho_{zz}(T)$, the temperature-dependent electrical resistivity with the current along the ab plane and the c axis. Bottom panel: $C_p(T)$, the temperature-dependent specific heat; and the zoom-in of $C_p(T)$ near transitions (inset). Note: the resistivity curves of $x = 0$ are from Ref. [11].
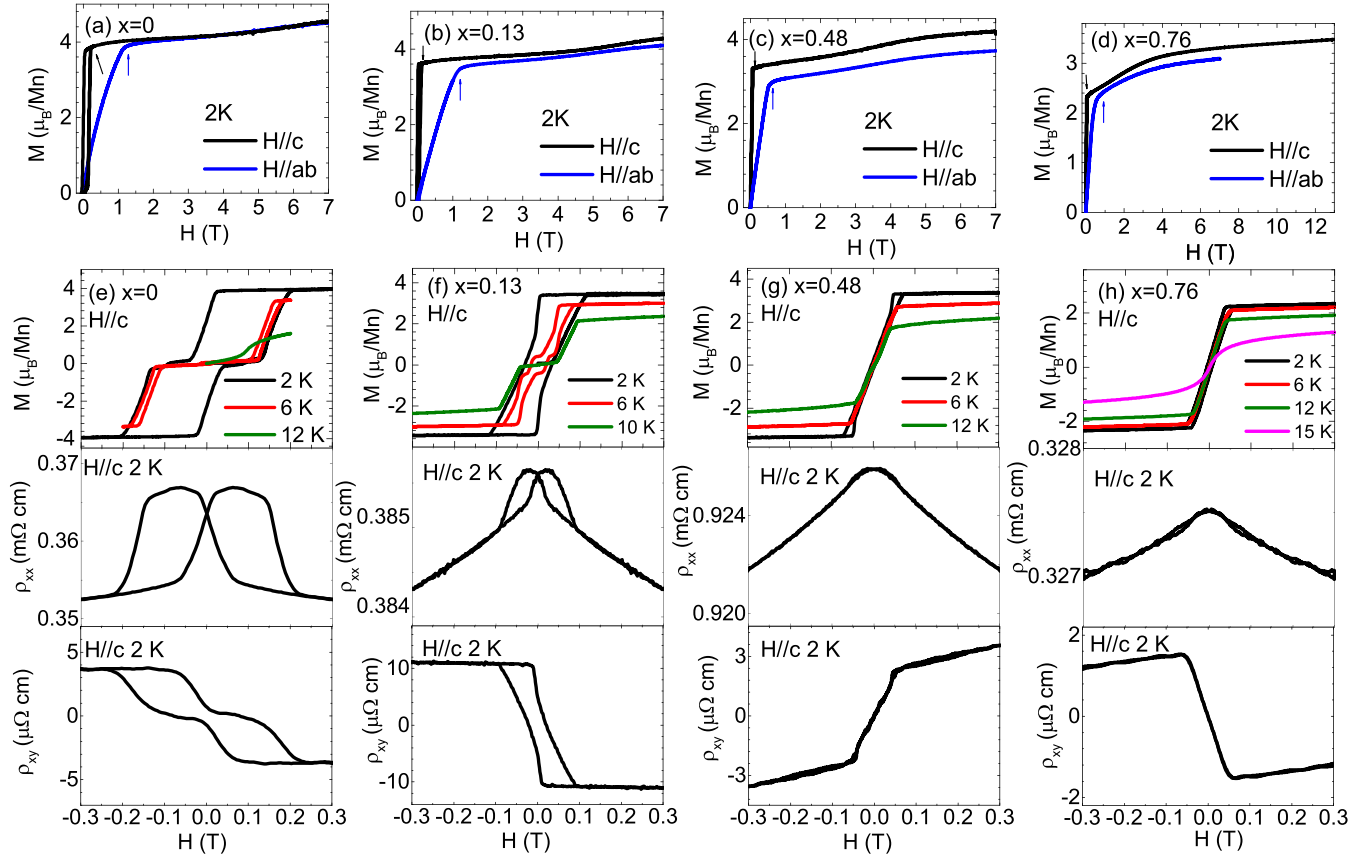
FIG. 3. Evolution of magnetism with field in $Mn(Bi_{1-x}Sb_x)_4Te_7$ from $x = 0$ to $x = 0.76$. (a)–(d) The isothermal magnetization $M(H)$ at 2 K with $H \parallel c$ and $H \parallel ab$. The unit is chosen as μ_B/Mn, where the Mn concentrations via WDS data are used. (e)–(h) The hysteresis of $M(H)$ (top), $\rho_{xx}(H)$ (middle), and $\rho_{xy}(H)$ (bottom) with $H \parallel c$ at 2 K (unless noted otherwise). At 2 K, the hysteresis of the $M(H)$ curve goes from AFM type ($x = 0$) to FM type ($x = 0.76$).

T_N to T_C, Mn1 and Mn2 sublattices each adopts A-type AFM, while they are also AFM coupled to each other. Below T_C, while Mn1 and Mn2 sublattices are still AFM coupled to each other, they are FM within themselves. We denote these two magnetic structures as $Ferri^{AFM}$ and $Ferri^{FM}$, as depicted in Fig. 4(a).

For $x = 0.48$, the shapes of the $\chi^c(T)$, $\rho_{zz}(T)$, and $\rho_{xx}(T)$ curves are similar to those of the $x = 0.13$ compound, manifesting a $Ferri^{AFM}$ state between $T_N = 13.3$ K and $T_C = 10.2$ K and a $Ferri^{FM}$ state below T_C. However, in sharp contrast to the $x = 0.13$ sample where a specific heat anomaly only appears at T_N, an additional small specific heat anomaly emerges at T_C for $x = 0.48$, indicating an entropy release which is not directly originated from the AFM-FM transition of the Mn1 and Mn2 sublattice at T_C. Since it is natural to believe that Mn3 concentration is higher in this doping level than that in the $x = 0.13$ sample, this additional specific heat release is very likely to be related to the increasing amount and the magnetic state of the Mn3 sublattice.

For $x \geqslant 0.58$ [Figs. S1(c) and S1(d) (see Supplemental Material [61]) and Fig. 2(d)], only one phase transition is observed. As a representative, the data for $x = 0.76$ is shown in Fig. 2(d). The $\chi^c(T)$, $\rho_{zz}(T)$, and $\rho_{xx}(T)$ are reminiscent of those of the $x = 0.13$ and 0.48 compounds in the $Ferri^{FM}$ state, suggesting Mn1 and Mn2 sublattices order simultaneously at 14.5 K into the $Ferri^{FM}$ state.

Figures 3(a)–3(d) present the isothermal magnetization data at 2 K under $H \parallel ab$ and $H \parallel c$. The data suggest an easy-c axis for the whole series. It also allows us to estimate the uniaxial anisotropy SD via $SD = (1/2)g\mu_B H_{ab} - g\mu_B H_c$ [36], where $g = 2$ and H_{ab} and H_c are the field marked by the arrows in the figures. The obtained SD is summarized in Table I. As we can see that SD decreases with high Sb doping, similar to the case of Sb-doped $MnBi_2Te_4$ [36]. Figures 3(e)–3(h) show the magnetic hysteresis loop, the field-dependent electrical resistivity [$\rho_{xx}(H)$], and Hall resistivity [$\rho_{xy}(H)$] with $H \parallel c$. A spin flip transition with hysteresis was observed at 0.15 T in the $x = 0$ sample. For $x = 0.13$, 0.37 [Fig. S1(b)], 0.48, and 0.58 [Fig. S1(d)] samples, the envelopes of the $M(H)$ curves in the $Ferri^{FM}$ ground state are nontrivial. Instead of a standard FM hysteresis loop, a bow-tie-shaped hysteresis loop can be clearly observed at 2 K. A recent magneto-optic study suggests this bow-tie-shaped hysteresis may be related to the formation of low-field fine-structured isotropic domains and high-field less isotropic sea-urchin-shaped domains [51]. We also note that the multistep feature of the $M(H)$ curve at 6 K for the $x = 0.13$ compound is reminiscent of that of the $MnBi_6Te_{10}$ compound [51]. This may suggest the existence of a small amount of FM domains in the AFM state of $MnBi_6Te_{10}$. Therefore, close energy scales of FM and AFM are universal in the $n \geqslant 2$ MBT members. This explains the controversies on the magnetic ground states of $MnBi_4Te_7$
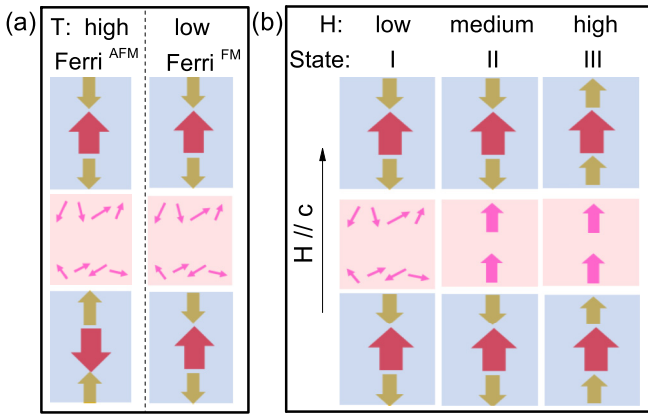
FIG. 4. (a) Depiction of the Ferri^{AFM} and Ferri^{FM} states. Red, olive, and pink arrows represent the Mn1, Mn2, and Mn3 spins. (b) Ferri^{FM} state with $H \parallel c$ at low, medium, and high field: the depiction of the process of the polarization of Mn3 and the spin flipping of Mn2.

obtained from different growth methods, while the first-principle calculations suggest an AFM ground state [11,20]. This is all because slight site defects are enough to tune the exchange energy to surrender one and boost the other.

Magnetism and charge carriers are strongly coupled in this series. At $x = 0$, a sharp drop in $\rho_{xx}(H)$ can be observed at the spin-flip field around 0.15 T due to the loss of spin-disorder scattering. On the other hand, $\rho_{xx}(H)$ shows a subtle decrease for the $x = 0.13, 0.48$, and 0.76 samples, consistent with their Ferri^{FM} ground state. In the Hall resistivity panels, anomalous Hall effect arising from the internal magnetization can be seen in all concentrations. Furthermore, a clear sign change of ordinary Hall resistivity appears at $x = 0.48$. We then determine the carrier density using $n = \frac{1}{R_H e}$, where the Hall coefficient R_H is the slope of $\rho_{xy}(H)$ at 20 K in Fig. S2(a). After interpolating the carrier density with doping level, an estimated charge neutrality point is found near $x = 0.36$, as shown in Fig. S2(b).

B. Defects and the magnetic state of the Mn3 sublattice

Based on our aforementioned discussions about Fig. 2, we have hypothesized the magnetic structures of the Mn1 and Mn2 sublattices. However, a few important questions remain unclear for this doping series. What are the concentrations of the Mn1, Mn2, and Mn3 sublattices? Does the Mn3 sublattice order? If yes, what is its ordering state? If not, is it glassy or fluctuating? Single-crystal neutron scattering measurements were performed on the $x = 0.76$ sample. Together with the high-field $M(H)$ data which provides an alternative way to estimate the concentrations of the three Mn sublattices, they shed light on these questions.

The preliminary refinement of the single-crystal neutron data with all fitting parameters free indeed indicates a Ferri^{FM} state of the Mn1 and Mn2 sublattice at 5 K, consistent with Fig. 4(a). The refinement further suggests the moment contributed from Mn3 atoms is 0.13(10)μ_B/f.u. This small moment either implies negligible Mn3 concentration or the Mn3 sublattice is glassy/fluctuating. To differentiate these

two scenarios, let us focus on the high-field $M(H)$ data with $H \parallel c$ shown in Figs. 3(a)–3(d). Above a sharp increase caused by the Mn1 + Mn2 complex below 0.2 T, a universal, subtle, but clear medium-field magnetization increase appears around 1–5 T in the whole doping series. Because the coupling between Mn1 and Mn3 is weaker than that between Mn1 and Mn2, Mn3 should polarize at a lower field than Mn2. Therefore, this medium-field magnetization increase should arise from the polarization of the Mn3 sublattice since the Mn2 sublattice will flip at a much higher field. Indeed, for $x = 0.76$, $M(H)$ is only 3.4μ_B/Mn at 13 T. Despite reaching a plateau, it is still much smaller than 5μ_B/Mn, the theoretical value for Mn^{2+}. This strongly indicates the flipping of Mn2 will happen at a field higher than 13 T. As a reference, in MnBi$_2$Te$_4$, the flipping process of the Mn2 sublattice starts at 20 T and ends at 60 T [52].

Such a field-dependent magnetic structure evolution is depicted in Fig. 4(b), which allows us to separate the contribution of magnetization from each Mn sublattice in the $M(H)$ curve with $H \parallel c$ [Figs. 3(a)–3(d)]. Right before the sizable polarization of the Mn3 sublattice, the sample is in the state I depicted in Fig. 4(b) and we denote the moment to be α. Then, with increasing field, more and more Mn3 atoms are polarized into the state II as pictured in Fig. 4(b), leading to a plateau in $M(H)$ with the moment of β. With even higher fields, Mn2 will be polarized and finally all three Mn sublattices stay in state III as drawn in Fig. 4(b), resulting in a moment of γ. Therefore, the difference in α and β can tell us the total moment contributed by Mn3 atoms under field. For $x = 0.76$, this value is $\sim 0.8(1)\mu_B$/Mn, suggesting the Mn3 spins contribute significantly to the ordered moment under fields and thus Mn3 concentration is not negligible. Together with the neutron scattering data which reveal all Mn3 atoms only contribute 0.13(10)μ_B/f.u. at zero field, we conclude that Mn3 atoms are in the glassy/fluctuating state at 5 K. Furthermore, considering that Mn3 atoms need above 1 T to be polarized while the recent ac susceptibility measurements of the $x = 0.76$ sample only show relaxation behavior below 500 Oe [53], it is likely that at 5 K the Mn3 atoms are not in the glassy state, but rather fluctuating in the paramagnetic state. Future site-sensitive nuclear magnetic resonance measurements can help clarify the magnetic state of the Mn3 sublattice.

According to the sequential field-induced processes illustrated in Fig. 4(b), we can quantitatively estimate the concentration of the three Mn sublattices based on the $M(H)$ data. If we set the amount of the Mn2 and Mn3 antisites and the Mn occupancy on the Mn1 site to be m, n, and l, respectively, then the concentration of the Mn1, Mn2, and Mn3 sublattices is $1 - l$, $2m$, and $2n$, with $2m + 2n + (1 - l) = $ Mn$^{\text{WDS}}$, where Mn$^{\text{WDS}}$ is the total Mn concentration determined by the WDS measurement. Assuming the ordered moment/Mn for Mn1, Mn2, and Mn3 is the same, we can readily write down a set of equations based on Fig. 4(b):

$$(l - 2m)/\text{Mn}^{\text{WDS}} = \alpha/\gamma, \qquad (1)$$

$$(l - 2m + 2n)/\text{Mn}^{\text{WDS}} = \beta/\gamma, \qquad (2)$$

$$(2m + 2n + l)/\text{Mn}^{\text{WDS}} = 1. \qquad (3)$$

TABLE II. Refined structural parameters for the $x = 0.76$ sample based on the single crystal neutron diffraction data measured at 50 K and 5 K.

Name	x	y	z	Occ.	Moment at 5 K
Mn1	0	0	0.5	0.623(4)	$4.6\mu_B/$Mn
Bi1	0	0	0.5	0	
Sb1	0	0	0.5	0.377(4)	
Bi2	0.333	0.667	0.342(1)	0.21(2)	
Sb2	0.333	0.667	0.342(1)	0.73(2)	
Mn2	0.333	0.667	0.342(1)	0.06(1)	$-4.6\mu_B/$Mn
Bi3	0.333	0.667	0.0842(1)	0.37(2)	
Sb3	0.333	0.667	0.0842(1)	0.56(2)	
Mn3	0.333	0.667	0.0842(1)	0.07	0
Te1	0	0	0	0.083	
Te2	0.333	0.667	0.155(1)	0.167	
Te3	0	0	0.273(1)	0.167	
Te4	0.333	0.667	0.430(1)	0.167	

For the $x = 0.76$ sample, $Mn^{WDS} = 0.82$. We take the moment at 1 T as α, where the subtle slope change in $M(H)$ suggests the onset of the polarization process of the Mn3 sublattice. We then take the moment at 13 T as β and assume $\gamma = 5\mu_B/$Mn. Using these values, we estimate m, n, and l to be 0.060(5), 0.07(1), and 0.56(3). For the other dopings, since $M(H)$ was only measured up to 7 T, we set β to be the moment at 7 T plus $0.1\mu_B/$Mn. The obtained m, n, and l are summarized in Table I.

Keeping the aforediscussed defect estimation in mind, next let us switch gear back to the neutron data. Quantitatively, since this is a doped system with multiple types of defects, we have to make several assumptions for the refinement. First, for the magnetic reflection data taken at 5 K, we fix the ordered moment of Mn3 as 0 and the concentration of Mn3 as 0.07; we then assume a fixed moment of $4.6\mu_B/$Mn for Mn1 and Mn2, the same value as that of the parent MnBi$_4$Te$_7$ obtained from neutron scattering [53]. By these restrictions, Mn1 and Mn2 occupancy are refined. Second, the Mn1 and Mn2 occupancies are then used for a more comprehensive structural refinement for the scattering data at 50 K to better determine the atomic coordinates and the Sb and Bi level. Such information is then fed back to the magnetic refinement of the 5 K data. A recursive process is repeated until all values converge. Eventually, the refinement with 27 reflections at 5 K yielded $R_F = 3.03\%$ and $\chi^2 = 1.99$; the refinement with 118 reflections at 50 K yielded $R_F = 2.16\%$ and $\chi^2 = 1.46$. The refinement result is summarized in Table II and Table I. Our refinement unambiguously shows site mixing. Opposite magnetic moments are observed in Mn1 and Mn2 sites, suggesting the Ferri^{FM} state. m is 0.06(1), l is 0.62(1), and the total Mn concentration is 0.88(3). Considering that the Mn3 concentration is fixed with no error in the neutron refinement which will lead to a smaller error bar in the total Mn concentration, these defect concentrations are consistent with the ones obtained from the $M(H)$ and WDS data. In addition, Sb atoms are found to be inhomogeneously doped in each site. The Sb has an overall higher concentration in the SLs than in QLs. In the Mn1 site, no Bi is found at all.

C. Band topology

To investigate the evolution of band topology for this series, DFT calculations are performed. For the $x = 0$ compound, the DFT calculations are made in the *A*-type AFM configuration. The presence of the band inversions in Fig. S3(a) hints toward a topological phase. To reveal the topological ground state of this system, we compute the topological invariant Z_2 index. In a general case, the Z_2 invariant is ill defined in a time-reversal symmetry breaking system. Nonetheless, Z_2 can be expanded to classify topological states in a magnetic system that possesses a specific magnetic configuration, for example, an *A*-type AFM state, in which the combinatory symmetry $S = \theta T_{1/2}$ exists, where θ is the time-reversal operator and $T_{1/2}$ is the half translational symmetry along the c axis of the AFM primitive cell [54–56]. The trajectory of Wannier charge centers (WCCs) is an open curve traversing the whole Brillouin zone (BZ) in the $k_z = 0$ plane via the Z_2 invariant by the Wilson loop method [Fig. S3(b)], indicating $Z_2 = 1$. Thus MnBi$_4$Te$_7$ is an antiferromagnetic topological insulator (AFM-TI), similar to the previous work [11].

For the doped compounds with FM ground states, we discuss two limiting cases. In case I, no defect is considered and FM configuration is used. In case II, a large amount of antisites are studied and the Ferri^{FM} order is used. For the sake of feasibility, in case II, we assume only Mn1 and Mn2 sublattices exist and 16.7% of Bi/Sb atoms in the SLs exchange with the Mn atoms on the same layer to form Mn2 antisites. The value is close to the antisite concentration in MnSb$_2$Te$_4$ [39], but much larger than that in our samples. Hence this will give an exaggerated effect of antisites.

Case I: Defect-free scenario

We first construct a tight-binding Hamiltonian for both FM MnBi$_4$Te$_7$ and MnSb$_4$Te$_7$ using our experimental lattice parameters in Fig. 1. Then the electronic structures of the doped compounds are calculated by a linear interpolation of tight-binding model matrix elements of the Hamiltonians. This approach was successfully applied to investigate the evolution of band topology in BiTlSe$_{1-x}$S$_x$ TI and Mo$_x$W$_{1-x}$Te$_2$ Weyl semimetal [57,58]. By that, the calculated band structure without defects is shown in Figs. 5(a)–5(e).

For all doping levels, a sizable band gap of 200–300 meV opens, with a band inversion between the (Bi, Sb)-p and Te-p states in the vicinity of E_F. Our topological invariant calculations show the Chern numbers to be zero both in the $k_z = 0$ and $k_z = \pi$ planes. Next, we compute the parity-based higher-order Z_4 invariant, which is defined by $Z_4 = \sum_{i=1}^{8}\sum_{n=1}^{n=occ}[(1 + \xi_n(\gamma_i)]2 \bmod 4$, where $\xi_n(\gamma_i)$ is the parity eigenvalue ($+1$ or -1) of the nth band at the ith time reversal invariant point Γ_i and $n = occ$ is the number of occupied bands [59]. The Z_4 invariant is well defined for an inversion symmetric system, even in the absence of time reversal symmetry. The odd values of Z_4 ($Z_4 = 1, 3$) indicate a Weyl semimetal phase, while $Z_4 = 2$ corresponds to an insulator phase with a quantized topological magnetoelectric effect (axion coupling $\theta = \pi$) [12,60]. Our calculation shows the Z_4 invariant of Mn(Bi$_{1-x}$Sb$_x$)$_4$Te$_7$ with FM configuration to be 2 for all x, which suggests a 3D FM axion insulator phase.
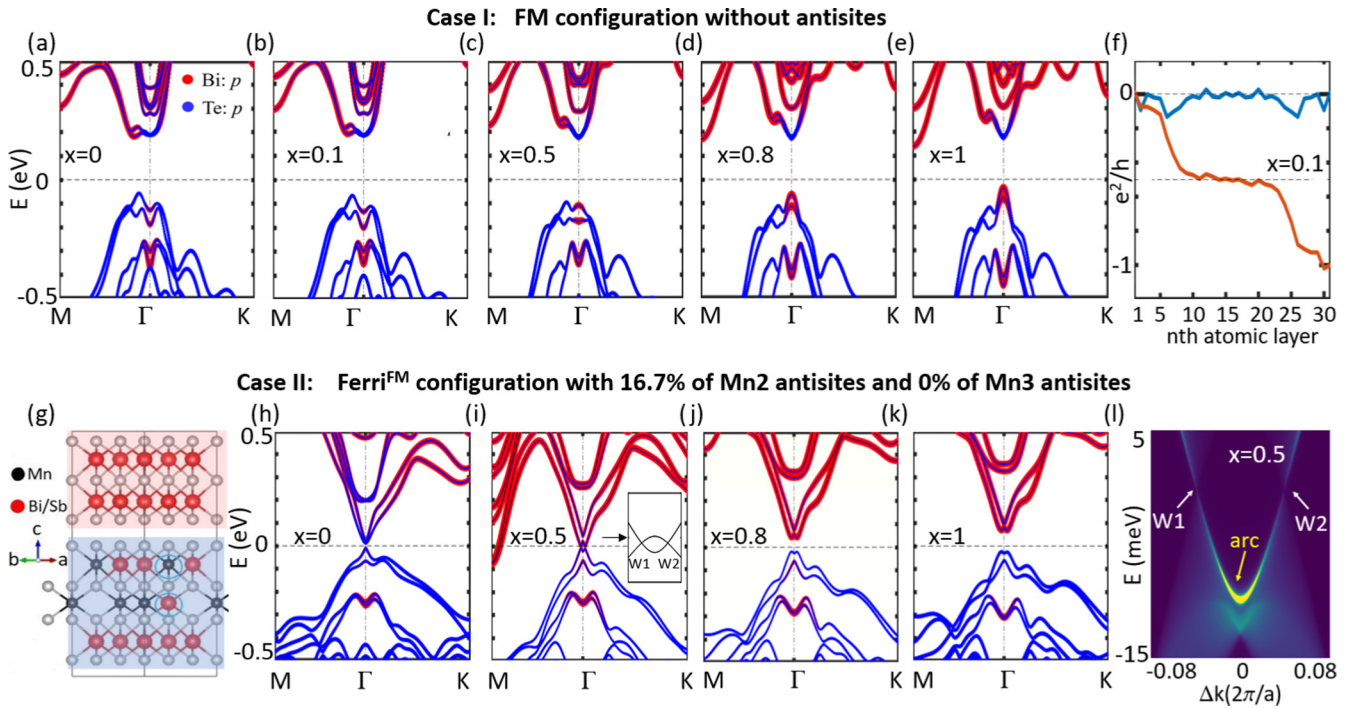
FIG. 5. (a)–(f) DFT calculations in the defect-free and FM configuration case. (a)–(e) Bulk band structures. The red and blue dots indicate (Bi,Sb)-p and Te-p orbitals, respectively. (f) Layer-resolved AHC for $x = 0.1$ sample. Partial AHC of each atomic layer (blue line); integral of the partial AHC (red line). (g)–(l) DFT calculations in the 16.7% of periodic Mn2 antisites and Ferri^{FM} configuration case. (g) The depiction of the structure model used. (h)–(k) Bulk band structures. (l) Surface band structure ($x = 0.5$) along the momentum space cut that goes through a direct pair of Weyl nodes W1 and W2.

To show the novel physics, taking the $x = 0.1$ compound as an example, we further investigate the anomalous Hall conductivity (AHC) in the 2D limit (Fig. S4). For a 31 atomic layer symmetric slab, vacuum-[SL-QL-SL-QL-SL]-vacuum, when the E_F is gated inside the energy band gap, the layer-resolved AHC calculation [the blue line in Fig. 5(f)] shows that the AHC mainly comes from the atomic layers on the top and bottom surfaces (about one SL and half QL), and the intensity rapidly decreases to approximately zero in the middle region of the device. As a result, each surface ($\lesssim 10$ atomic layers) contributes [the red line in Fig. 5(f)] $-0.5e^2/h$ to AHC, and gives $-1e^2/h$ for the whole slab. The half-integer quantized plateau in the middle indicates that the axion coupling strength equals the quantization value of π in this device, further confirming the $x = 0.1$ compound as a FM axion insulator [62].

Case II: Periodic Mn2-antisite scenario

To include the antisite effect in case II, we perform the supercell calculation. First, we construct a $\sqrt{3} \times \sqrt{3}$ supercell of MnBi$_4$Te$_7$. In this model, one atomic Mn layer contains three Mn atoms (Mn1 sublattice). Then we exchange one Mn atom and one Bi atom within the SL (Mn2 sublattice), resulting in a chemical formula of (Mn$_{0.67}$ Bi$_{0.33}$) (Bi$_{0.833}$ Mn$_{0.167}$)$_2$Te$_4$ · Bi$_2$Te$_3$ as shown in Fig. 5(g). By this, we calculate the band structure of MnBi$_4$Te$_7$ with 16.7% of the antisite disorder. We then perform a similar

procedure to calculate the band structure of (Mn$_{0.67}$ Sb$_{0.33}$) (Sb$_{0.833}$ Mn$_{0.167}$)$_2$Te$_4$ · Sb$_2$Te$_3$. Finally, electronic structures of the doped compounds are calculated by a linear interpolation of tight-binding model matrix elements of the Bi and Sb versions.

Our calculation indeed shows that, in this defect limit, the magnetic configuration of Mn1 and Mn2 is FM individually, while Mn1 and Mn2 are coupled antiferromagnetically, forming the Ferri^{FM} ground state. In the Ferri^{FM} state, the bulk band gap of MnBi$_4$Te$_7$ is greatly reduced to about 20 meV. Meanwhile, the character of the band inversion also alters with doping, as shown in Figs. 5(h)–5(k). Consequently, in the intermediate doping region at $x = 0.5$, for example, one can see a small energy gap about 10 meV near the Γ point [inset of Fig. 5(i)]. This tiny gap implies the existence of a Weyl semimetal state. Since the gapless Weyl points are not guaranteed to locate on the high symmetry point or the high symmetry line, to confirm the chirality of the Weyl nodes, we calculate the chiral charge based on the Wilson loop method. The associated chiral charge for W1(W2) is calculated to be $-1(+1)$ based on the Wilson loop method (Fig. S5), indicating that they carry opposite chirality and do form a pair of Weyl nodes. Furthermore, a topological Fermi arc state, the characteristics of Weyl semimetal, appears in the (100) surface states and terminates directly at the projected Weyl nodes [Fig. 5(l)]. This further supports the picture of a ferrimagnetic type-I Weyl semimetal with only two Weyl nodes.
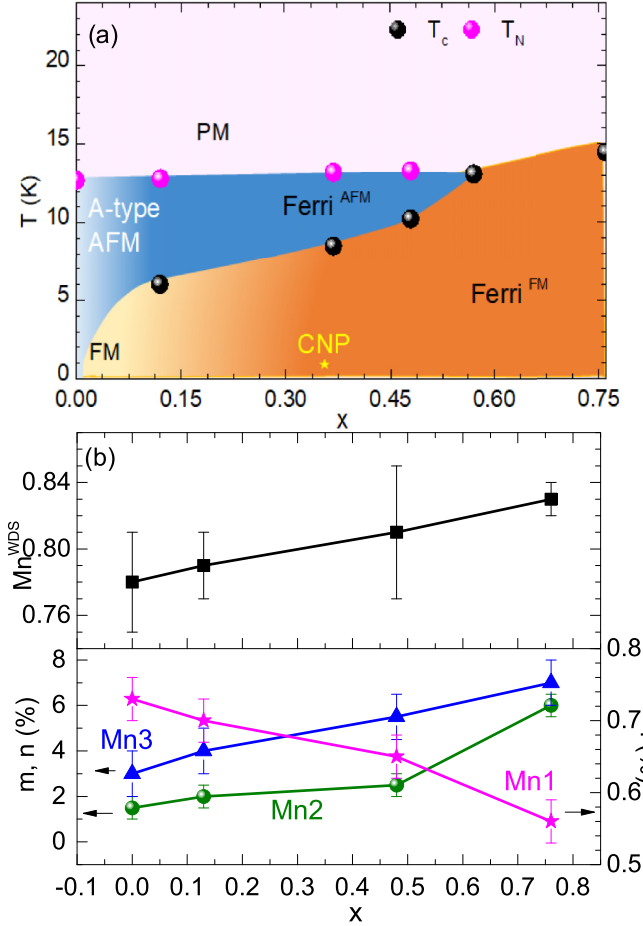
FIG. 6. (a) Temperature-doping (T-x) phase diagram. With increasing x, the carrier-type changes from electron to hole. A linear fitting with our data (Fig. S2) yields a charge neutrality point (CNP) near $x = 0.36$. (b) The doping-dependent Mn^{WDS}, m, n, and l.

IV. DISCUSSION

As shown in Fig. 6(b), Sb doping leads to a decrease in the Mn1 concentration; meanwhile, it also boosts the number of Mn2 and Mn3 antisites, leading to an overall enhanced Mn^{WDS}. This defect evolution is responsible for the evolvement of magnetism, as summarized by the temperature-doping phase diagram in Fig. 6(a).

We argue that the AFM to FM transition of the dominate Mn1 sublattice arises from the delicate competitions between the direct Mn1-Mn1 AFM interlayer interaction and Mn3-assisted Mn1-Mn1 FM interlayer coupling. The magnetic Hamiltonian may be approximated as follows. The Mn1 sublattice itself has strong FM intralayer couplings J_0 and weak interlayer AFM interactions J_1. The Mn2 and Mn3 sublattices are so sparse that the interactions among themselves are negligible, but they couple to Mn1 through strong superexchange interactions J_2 and J_3 due to their proximity. Finally, there is Mn2-Mn3 coupling, which modifies J_3 into J_3^{eff}. Note that the sign of J_3^{eff} can vary from site to site (for instance, depending on whether the closest Mn neighbor to a Mn is Mn1 or Mn2).

Now, while Mn2 just follows Mn1 and does not affect the overall Mn1-Mn1 interlayer ordering, Mn3 introduces an effective FM interlayer coupling when they couple to the neighboring Mn1 layers above and below:

$$H_{interlayer} = J_1 \langle \mathbf{M}_1 \cdot \mathbf{M}_1' \rangle + \langle J_3^{eff} (\mathbf{M}_1 \cdot \mathbf{M}_3 + \mathbf{M}_1' \cdot \mathbf{M}_3) \rangle, \quad (4)$$

where $\mathbf{M}_1$ and $\mathbf{M}_1'$ are the local magnetizations of the two neighboring Mn1 layers, $\mathbf{M}_3$ is the local magnetization of the Mn3 bilayer between these Mn1 layers, and the brackets denote the average of the ab plane. The second term equals 0, if the Mn1 sublattice is AFM, and $-2\langle |J_3^{eff} M_3 M_1| \rangle$, if the Mn1 sublattice is FM, regardless of the sign of J_3^{eff}; thus it always favors the FM ordering of the Mn1 sublattice (that is, the Mn3 mediates FM interlayer coupling of the Mn1 sublattice). We can see that, if $2c_3 |J_3^{eff} M_3| > c_1 J_1 M_1$, the system orders into the $Ferri^{FM}$ state with the energy $E_1 = c_1 J_1 M_1^2 - 2c_3 |J_3^{eff} M_3 M_1|$ and otherwise into the $Ferri^{AFM}$ state with $E_2 = -c_1 J_1 M_1^2$, where c_1 and c_3 are the concentrations of the Mn1 and Mn3 sublattice.

This consideration implicitly implies that the susceptibility of the Mn3 subsystem is infinite, which would be true at $T = 0$, and if the Mn3-Mn3 interaction can be neglected. Our neutron scattering indicates that Mn3 spins are strongly fluctuating, which suggests that the susceptibility of this subsystem, χ_{Mn3}, is finite. This does not change the conclusions qualitatively; the only change is that, if χ_{Mn3} is relatively small, the net Mn3 subsystem magnetization M_3 becomes proportional to $M_1 \chi_{Mn3}(T)$, and thus explicitly T dependent.

With this in mind, we can explain both the temperature and doping evolution of the magnetism. Because of the Mermin-Wagner physics, M_1 only weakly depends on T except close to T_N. Meanwhile, as long as the concentration of Mn3 remains low, Mn3 can be treated as free spins in an external field (the molecular field induced by Mn1) with $M_3 \propto \chi_{Mn3}(T) \propto 1/T$. Thus, upon cooling, the effective FM interaction increases much faster than the AFM, resulting in a $Ferri^{AFM}$ to $Ferri^{FM}$ transition at $T_C < T_N$ once $2c_3 |J_3^{eff} M_3| > c_1 J_1 M_1$. Furthermore, Fig. 6(b) and the comparison of the neutron refinements of the $x = 0$ [27] and $x = 0.76$ samples all indicate that c_3 increases and c_1 decreases with Sb doping. Therefore, inevitably, in the $T - x$ phase diagram, three doping regimes can appear: low doping region where the $Ferri^{AFM}$ state is stable at any temperature, high doping region when only the $Ferri^{FM}$ state is stable, and intermediate doping region, where the $Ferri^{FM}$ state is stable only up to some $T_C < T_N$ with T_C increasing with x. This doping dependence is exactly what we have observed in Fig. 6(a).

We note that l decreases with increasing x, so, besides the formation of antisites, Sb doping also leads to the magnetic dilution effect of the Mn1 sublattice. Future doping studies, such as Pb, Sn, or Ge substitution on the Mn site, if they will not cause antisite defects as the Sb doping does, may provide a cleaner platform to investigate the magnetic dilution effect on the magnetism in the MBT family.

Now let us turn our discussion to the band topology. It remains an open but important question how robust the nontrivial band topology and thus the associated emergent phenomena will be against the antisite defects. Recent studies showed that Mn antisites are universal in MBT: $\sim$3(1)% for $MnBi_2Te_4$ and $\sim$13%–16% for $MnSb_2Te_4$ [39,52]. While it is impossible to construct a structure model to reflect the real and complex chemical defects in our DFT calculations, our

attempts with the defect-free and periodic-Mn2-antisites scenarios shed light on this puzzle. Two insightful observations can be made from Fig. 5. First, in case II, the effect of Mn2 antisites is exaggerated on the band topology, especially for the low and intermediate dopings where the antisite defects are significantly smaller than 16.7%. However, even in this high-concentration case with periodic antisites, our calculations show robust band inversion and nontrivial topology, resulting in a Weyl semimetal state at the intermediate dopings. Second, in the Bi-rich side, the characteristics of the band inversion are very similar for the two cases [Figs. 5(a) and 5(h)]. However, in the Sb-rich side, the features of band inversion are apparently different [Figs. 5(e) and 5(k)]. This observation implies that the antisite defect has stronger effect on modifying the band topology in the Sb-rich 147 phase than the Bi-rich 147 phase. Therefore, we believe that the nontrivial topology is likely robust against the small amount of antisite defects here, especially at the Bi-rich side. Our finding is consistent with the observation that, despite 3(1)% of antisite defects, a zero-field QAH effect appears at 1.5 K in a 5-SL device of $MnBi_2Te_4$ [22]. Future systematic ARPES measurements, in combination with the DFT calculations on Sb-doped $MnBi_4Te_7$, will help settle this outstanding question.

V. CONCLUSION

In Sb-doped $MnBi_4Te_7$, the competition of the Mn1-Mn1 AFM interlayer coupling and the Mn3-assisted Mn1-Mn1 FM interlayer interaction leads to lower-temperature $Ferri^{FM}$ state and higher-temperature $Ferri^{AFM}$ state, where the Mn3 sublattice is dynamically fluctuating at all temperatures. Meanwhile, the nontrivial band topology appears robust against low or intermediate antisites, especially in the Bi-rich end, pointing to a kaleidoscope of magnetic topological phases including the FM axion insulator state at low Sb dopings and possible type-I ferrimagnetic Weyl semimetal states at intermediate Sb dopings.

[1] Y. Tokura, K. Yasuda, and A. Tsukazaki, Nat. Rev. Phys. **1**, 126 (2019).

[2] K. He, Y. Wang, and Q.-K. Xue, Annu. Rev. Condens. Matter Phys. **9**, 329 (2018).

[3] C.-X. Liu, S.-C. Zhang, and X.-L. Qi, Annu. Rev. Condens. Matter Phys. **7**, 301 (2016).

[4] J. Wang, B. Lian, X.-L. Qi, and S.-C. Zhang, Phys. Rev. B **92**, 081107(R) (2015).

[5] D. S. Lee, T.-H. Kim, C.-H. Park, C.-Y. Chung, Y. S. Lim, W.-S. Seo, and H.-H. Park, CrystEngComm **15**, 5532 (2013).

[6] E. Rienks, S. Wimmer, J. Sánchez Barriga, O. Caha, P. Mandal, J. Růžička, A. Ney, H. Steiner, V. Volobuev, H. Groiss et al., Nature (London) **576**, 423 (2019).

[7] D. Zhang, M. Shi, T. Zhu, D. Xing, H. Zhang, and J. Wang, Phys. Rev. Lett. **122**, 206401 (2019).

[8] J. Li, Y. Li, S. Du, Z. Wang, B.-L. Gu, S.-C. Zhang, K. He, W. Duan, and Y. Xu, Sci. Adv. **5**, eaaw5685 (2019).

[9] M. M. Otrokov, I. I. Klimovskikh, H. Bentmann, D. Estyunin, A. Zeugner, Z. S. Aliev, S. Gaß, A. Wolter, A. Koroleva, A. M. Shikin et al., Nature (London) **576**, 416 (2019).

[10] Z. S. Aliev, I. R. Amiraslanov, D. I. Nasonova, A. V. Shevelkov, N. A. Abdullayev, Z. A. Jahangirli, E. N. Orujlu, M. M. Otrokov, N. T. Mamedov, M. B. Babanly et al., J. Alloys Compd. **789**, 443 (2019).

[11] C. Hu, K. N. Gordon, P. Liu, J. Liu, X. Zhou, P. Hao, D. Narayan, E. Emmanouilidou, H. Sun, Y. Liu et al., Nat. Commun. **11**, 97 (2020).

[12] C. Hu, L. Ding, K. N. Gordon, B. Ghosh, H.-J. Tien, H. Li, A. G. Linn, S.-W. Lien, C.-Y. Huang, S. Mackey et al., Sci. Adv. **6**, eaba4275 (2020).

[13] H. Deng, Z. Chen, A. Wołoś, M. Konczykowski, K. Sobczak, J. Sitnicka, I. V. Fedorchenko, J. Borysiuk, T. Heider, ŁL. Pluciński, K. Park, A. B. Georgescu, J. Cano, and L. Krusin Elbaum, Nat. Phys. **17**, 36 (2020).

[14] Y. Gong, J. Guo, J. Li, K. Zhu, M. Liao, X. Liu, Q. Zhang, L. Gu, L. Tang, X. Feng et al., Chin. Phys. Lett. **36**, 076801 (2019).

[15] S. H. Lee, Y. Zhu, Y. Wang, L. Miao, T. Pillsbury, H. Yi, S. Kempinger, J. Hu, C. A. Heikes, P. Quarterman et al., Phys. Rev. Research **1**, 012011(R) (2019).

[16] J.-Q. Yan, Q. Zhang, T. Heitmann, Z. Huang, K. Y. Chen, J.-G. Cheng, W. Wu, D. Vaknin, B. C. Sales, and R. J. McQueeney, Phys. Rev. Materials **3**, 064202 (2019).

[17] A. Zeugner, F. Nietschke, A. U. Wolter, S. Gaß, R. C. Vidal, T. R. Peixoto, D. Pohl, C. Damm, A. Lubk, R. Hentrich et al., Chem. Mater. **31**, 2795 (2019).

[18] M. M. Otrokov, I. P. Rusinov, M. Blanco-Rey, M. Hoffmann, A. Y. Vyazovskaya, S. V. Eremeev, A. Ernst, P. M. Echenique, A. Arnau, and E. V. Chulkov, Phys. Rev. Lett. **122**, 107202 (2019).

[19] B. Chen, F. Fei, D. Zhang, B. Zhang, W. Liu, S. Zhang, P. Wang, B. Wei, Y. Zhang, Z. Zuo *et al.*, Nat. Commun. **10**, 1 (2019).

[20] J. Wu, F. Liu, M. Sasase, K. Ienaga, Y. Obata, R. Yukawa, K. Horiba, H. Kumigashira, S. Okuma, T. Inoshita *et al.*, Sci. Adv. **5**, eaax9989 (2019).

[21] Y.-J. Hao, P. Liu, Y. Feng, X.-M. Ma, E. F. Schwier, M. Arita, S. Kumar, C. Hu, R. Lu, M. Zeng *et al.*, Phys. Rev. X **9**, 041038 (2019).

[22] Y. Deng, Y. Yu, M. Z. Shi, Z. Guo, Z. Xu, J. Wang, X. H. Chen, and Y. Zhang, Science **367**, 895 (2020).

[23] C. Liu, Y. Wang, H. Li, Y. Wu, Y. Li, J. Li, K. He, Y. Xu, J. Zhang, and Y. Wang, Nat. Mater. **19**, 522 (2020).

[24] Y. J. Chen, L. X. Xu, J. H. Li, Y. W. Li, H. Y. Wang, C. F. Zhang, H. Li, Y. Wu, A. J. Liang, C. Chen *et al.*, Phys. Rev. X **9**, 041040 (2019).

[25] H. Li, S.-Y. Gao, S.-F. Duan, Y.-F. Xu, K.-J. Zhu, S.-J. Tian, J.-C. Gao, W.-H. Fan, Z.-C. Rao, J.-R. Huang *et al.*, Phys. Rev. X **9**, 041039 (2019).

[26] B. Li, J.-Q. Yan, D. M. Pajerowski, E. Gordon, A.-M. Nedić, Y. Sizyuk, L. Ke, P. P. Orth, D. Vaknin, and R. J. McQueeney, Phys. Rev. Lett. **124**, 167204 (2020).

[27] L. Ding, C. Hu, F. Ye, E. Feng, N. Ni, and H. Cao, Phys. Rev. B **101**, 020412(R) (2020).

[28] M. Z. Shi, B. Lei, C. S. Zhu, D. H. Ma, J. H. Cui, Z. L. Sun, J. J. Ying, and X. H. Chen, Phys. Rev. B **100**, 155144 (2019).

[29] S. Tian, S. Gao, S. Nie, Y. Qian, C. Gong, Y. Fu, H. Li, W. Fan, P. Zhang, T. Kondo, S. Shin, J. Adell, H. Fedderwitz, H. Ding, Z. Wang, T. Qian, and H. Lei, Phys. Rev. B **102**, 035144 (2020).

[30] J.-Q. Yan, Y. H. Liu, D. S. Parker, Y. Wu, A. A. Aczel, M. Matsuda, M. A. McGuire, and B. C. Sales, Phys. Rev. Materials **4**, 054202 (2020).

[31] K. N. Gordon, H. Sun, C. Hu, A. G. Linn, H. Li, Y. Liu, P. Liu, S. Mackey, Q. Liu, N. Ni *et al.*, arXiv:1910.13943.

[32] Y. Hu, L. Xu, M. Shi, A. Luo, S. Peng, Z. Y. Wang, J. J. Ying, T. Wu, Z. K. Liu, C. F. Zhang *et al.*, Phys. Rev. B **101**, 161113(R) (2020).

[33] L. Xu, Y. Mao, H. Wang, J. Li, Y. Chen, Y. Xia, Y. Li, J. Zhang, H. Zheng, K. Huang *et al.*, Sci. Bull. **65**, 2086 (2020).

[34] N. H. Jo, L.-L. Wang, R.-J. Slager, J. Yan, Y. Wu, K. Lee, B. Schrunk, A. Vishwanath, and A. Kaminski, Phys. Rev. B **102**, 045130 (2020).

[35] I. I. Klimovskikh, M. M. Otrokov, D. Estyunin, S. V. Eremeev, S. O. Filnov, A. Koroleva, E. Shevchenko, V. Voroshnin, A. G. Rybkin, I. P. Rusinov *et al.*, npj Quantum Mater. **5**, 1 (2020).

[36] J.-Q. Yan, S. Okamoto, M. A. McGuire, A. F. May, R. J. McQueeney, and B. C. Sales, Phys. Rev. B **100**, 104409 (2019).

[37] W. Ko, M. Kolmer, J. Yan, A. D. Pham, M. Fu, F. Lüpke, S. Okamoto, Z. Gai, P. Ganesh, and A.-P. Li, Phys. Rev. B **102**, 115402 (2020).

[38] T. Murakami, Y. Nambu, T. Koretsune, G. Xiangyu, T. Yamamoto, C. M. Brown, and H. Kageyama, Phys. Rev. B **100**, 195103 (2019).

[39] Y. Liu, L.-L. Wang, Q. Zheng, Z. Huang, X. Wang, M. Chi, Y. Wu, B. C. Chakoumakos, M. A. McGuire, B. C. Sales *et al.*, Phys. Rev. X **11**, 021033 (2021).

[40] M.-H. Du, J. Yan, V. R. Cooper, and M. Eisenbach, Adv. Funct. Mater. **31**, 2006516 (2021).

[41] J. Wu, F. Liu, C. Liu, Y. Wang, C. Li, Y. Lu, S. Matsuishi, and H. Hosono, Adv. Mater. **32**, 2001815 (2020).

[42] B. C. Chakoumakos, H. Cao, F. Ye, A. D. Stoica, M. Popovici, M. Sundaram, W. Zhou, J. S. Hicks, G. W. Lynn, and R. A. Riedel, J. Appl. Crystallogr. **44**, 655 (2011).

[43] J. Rodríguez-Carvajal, Phys. B: Condens. Matter **192**, 55 (1993).

[44] P. E. Blöchl, Phys. Rev. B **50**, 17953 (1994).

[45] G. Kresse and D. Joubert, Phys. Rev. B **59**, 1758 (1999).

[46] G. Kresse and J. Furthmüller, Comput. Mater. Sci. **6**, 15 (1996).

[47] J. P. Perdew, K. Burke, and M. Ernzerhof, Phys. Rev. Lett. **77**, 3865 (1996).

[48] S. Dudarev, G. Botton, S. Y. Savrasov, Z. Szotek, W. Temmerman, and A. Sutton, Phys. Status Solidi A **166**, 429 (1998).

[49] N. Marzari and D. Vanderbilt, Phys. Rev. B **56**, 12847 (1997).

[50] M. Winter, Webelements™, http://www.webelements.com/.

[51] C. Hu, M. A. Tanatar, R. Prozorov, and N. Ni, arXiv:2106.08969.

[52] Y. Lai, L. Ke, J. Yan, R. D. McDonald, and R. J. McQueeney, Phys. Rev. B **103**, 184429 (2021).

[53] L. Ding, C. Hu, E. Feng, C. Jiang, I. A. Kibalin, A. Gukasov, M. Chi, N. Ni, and H. Cao, J. Phys. D **54**, 174003 (2021).

[54] R. S. K. Mong, A. M. Essin, and J. E. Moore, Phys. Rev. B **81**, 245209 (2010).

[55] C. Fang, M. J. Gilbert, and B. A. Bernevig, Phys. Rev. B **88**, 085406 (2013).

[56] X. Gui, I. Pletikosic, H. Cao, H.-J. Tien, X. Xu, R. Zhong, G. Wang, T.-R. Chang, S. Jia, T. Valla *et al.*, ACS Central Sci. **5**, 900 (2019).

[57] S.-Y. Xu, Y. Xia, L. Wray, S. Jia, F. Meier, J. Dil, J. Osterwalder, B. Slomski, A. Bansil, H. Lin *et al.*, Science **332**, 560 (2011).

[58] T.-R. Chang, S.-Y. Xu, G. Chang, C.-C. Lee, S.-M. Huang, B. Wang, G. Bian, H. Zheng, D. S. Sanchez, I. Belopolski *et al.*, Nat. Commun. **7**, 10639 (2016).

[59] A. M. Turner, Y. Zhang, R. S. K. Mong, and A. Vishwanath, Phys. Rev. B **85**, 165120 (2012).

[60] B. J. Wieder and B. A. Bernevig, arXiv:1810.02373.

[61] See Supplemental Material at http://link.aps.org/supplemental/10.1103/PhysRevB.104.054422 for additional doping levels and supplementary data on magnetic, electronic and topological properties.

[62] N. Varnava and D. Vanderbilt, Phys. Rev. B **98**, 245117 (2018).

Tuning the magnetism and band topology through antisite defects in Sb doped MnBi₄Te₇

Chaowei Hu,[1,*] Shang-Wei Lien,[2,*] Erxi Feng,[3] Scott Mackey,[1] Hung-Ju Tien,[2] Igor I. Mazin,[4] Huibo Cao,[3] Tay-Rong Chang,[2, 5, 6, †] and Ni Ni[1,‡]

[1]Department of Physics and Astronomy and California NanoSystems Institute, University of California, Los Angeles, CA 90095, USA

[2]Department of Physics, National Cheng Kung University, Tainan 701, Taiwan

[3]Neutron Scattering Division, Oak Ridge National Laboratory, Oak Ridge, Tennessee 37831, USA

[4]Department of Physics and Astronomy, and Center of Quantum Science and Engineering, George Mason University, Fairfax, VA 22030, USA

[5]Center for Quantum Frontiers of Research and Technology (QFort), Tainan 701, Taiwan

[6]Physics Division, National Center for Theoretical Sciences, National Taiwan University, Taipei, Taiwan

1. Magnetic properties

Figure S1 presents the magnetic properties of the x=0.37 and 0.58 sample. They have a small amount of detectable Bi_2Te_3 phase impurities. For the x=0.37 sample, the susceptibility resembles those of x=0.13 and 0.48 with Tc=8.5 K and T_N=13.2 K. For x=0.58, the susceptibility is similar to that of x=0.76 but with a Tc of 13.6 K. Both magnetization curves at 2 K show a bow-tie shape that indicates Ferri[FM] ground state with the presence of AFM domains at low temperatures.
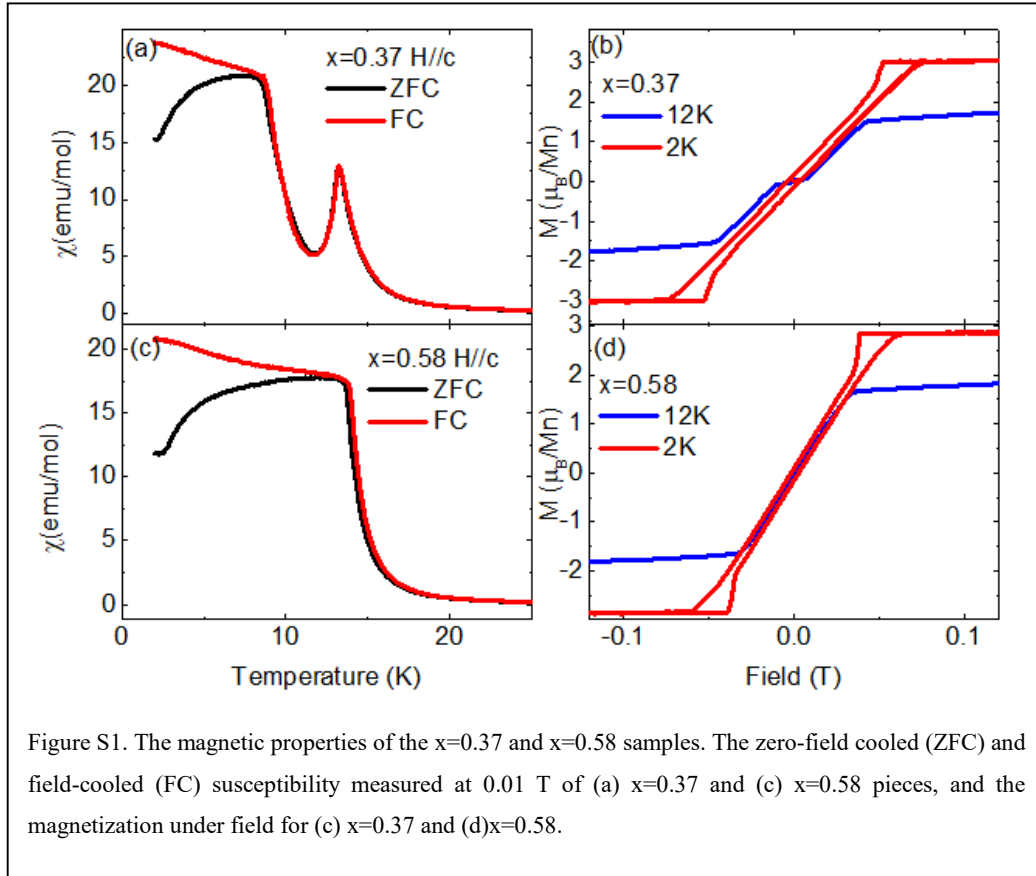

Figure S1. The magnetic properties of the x=0.37 and x=0.58 samples. The zero-field cooled (ZFC) and field-cooled (FC) susceptibility measured at 0.01 T of (a) x=0.37 and (c) x=0.58 pieces, and the magnetization under field for (c) x=0.37 and (d)x=0.58.
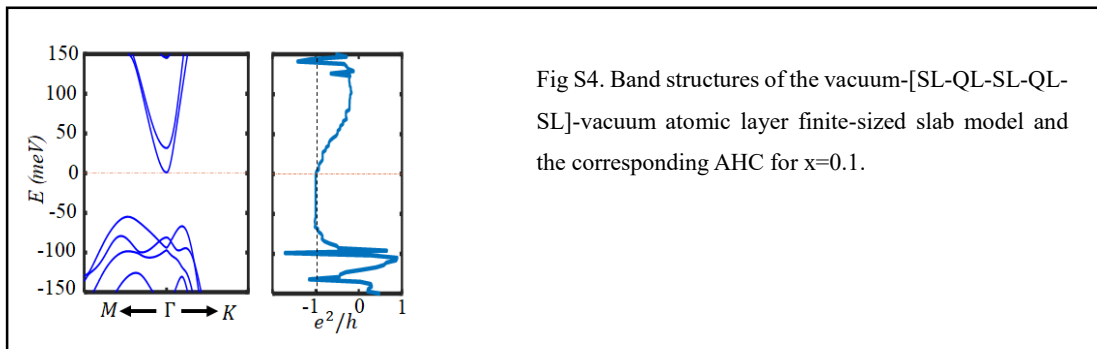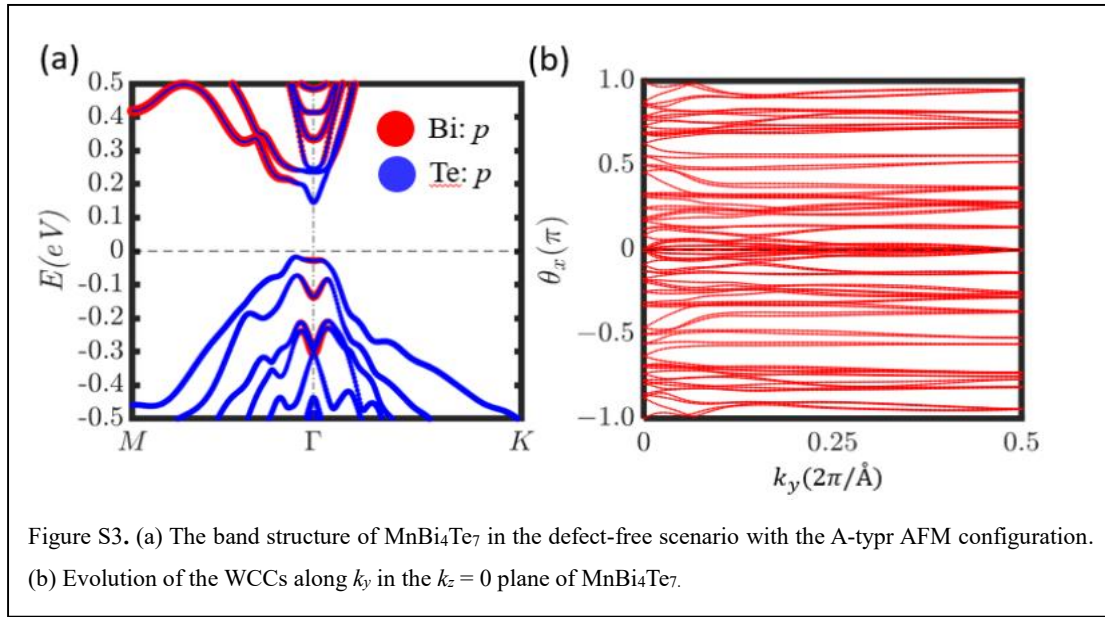
2. Carrier density

Figure S2(a) shows the Hall resistivity at 20 K. The range between 1 T to 9 T is used for the fitting to determine the carrier density. The obtained carrier density is summarized in Fig. S2(b). As we can see, upon Sb doping, the doped compound goes from electron-type to hole-type with the charge neutrality point at x=0.36.

Figure S2. (a) Hall resistivity measured at 20 K with I//ab. (b) Doping-dependent carrier density.
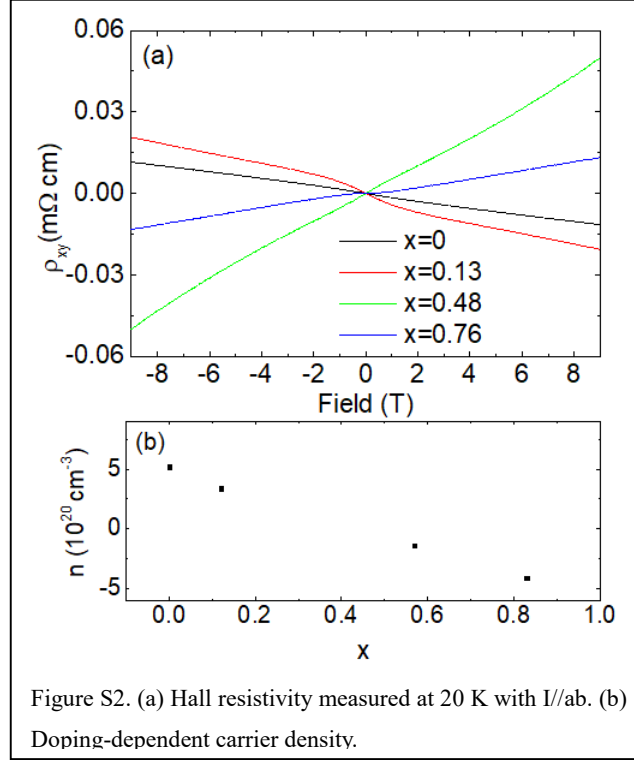
3. First-principles calculations

We computed the electronic structures using the projector augmented wave method [1,2] as implemented in the VASP package [3] within the generalized gradient approximation schemes (GGA) [4] and GGA plus Hubbard U (GGA + U) [5] scheme. On-site U = 5.0 eV was used for Mn d orbitals. A 11×11×5 MonkhorstPack k-point mesh was used in the computations. The spin-orbit coupling effects were included in calculations. The experimental lattice parameters were used. The atomic positions were relaxed until the residual forces were less than 0.01 eV/Å. We used Mn d orbitals, Bi p orbitals, Sb p orbitals, and Te p orbitals to construct Wannier functions, without performing the procedure for maximizing localization [6].
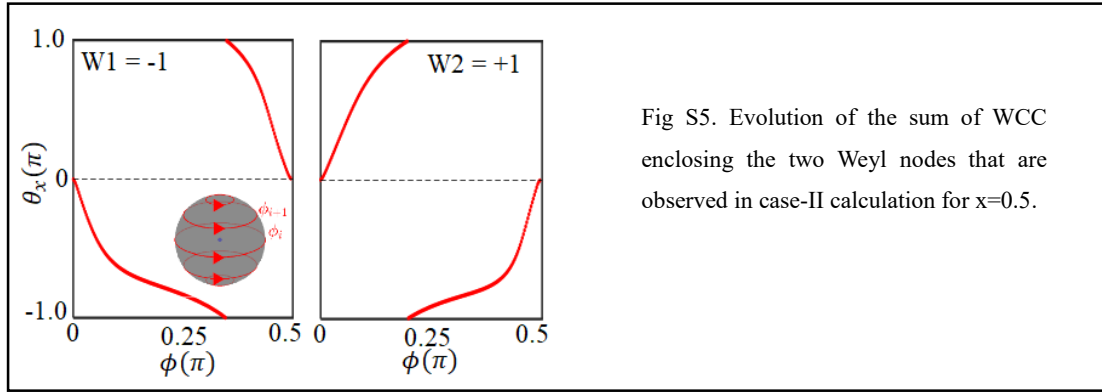
Figure S3. (a) The band structure of MnBi$_4$Te$_7$ in the defect-free scenario with the A-typr AFM configuration. (b) Evolution of the WCCs along k_y in the $k_z = 0$ plane of MnBi$_4$Te$_7$.

Fig S4. Band structures of the vacuum-[SL-QL-SL-QL-SL]-vacuum atomic layer finite-sized slab model and the corresponding AHC for x=0.1.

Fig S5. Evolution of the sum of WCC enclosing the two Weyl nodes that are observed in case-II calculation for x=0.5.

References

[1] P. E. Blöchl, *Projector Augmented-Wave Method*, Physical Review B **50**, 17953 (1994).

[2] G. Kresse and D. Joubert, *From Ultrasoft Pseudopotentials to the Projector Augmented-Wave Method*, Physical Review B **59**, 1758 (1999).

[3] G. Kresse and J. Furthmüller, *Efficiency of Ab-Initio Total Energy Calculations for Metals and Semiconductors Using a Plane-Wave Basis Set*, Computational Materials Science **6**, 15 (1996).

[4] J. P. Perdew, K. Burke, and M. Ernzerhof, *Generalized Gradient Approximation Made Simple*, Phys. Rev. Lett. **77**, 3865 (1996).

[5] S. Dudarev, G. Botton, S. Savrasov, C. Humphreys, and A. Sutton, *Electron-Energy-Loss Spectra and the Structural Stability of Nickel Oxide: An LSDA+ U Study*, Physical Review B **57**, 1505 (1998).

[6] N. Marzari and D. Vanderbilt, *Maximally Localized Generalized Wannier Functions for Composite Energy Bands*, Physical Review B **56**, 12847 (1997).